physics

MDPI

Article

Electro-Optical Modulation of the Nonlinear Optical Response in a GaAs/AlGaAs Symmetric Multiple Quantum Well System

Carlos Alberto Dagua-Conda [1,*], John Alexander Gil-Corrales [2], Rebeca Victoria Herrero-Hahn [3], Miguel Eduardo Mora-Ramos [4], Alvaro Luis Morales [1] and Carlos Alberto Duque [1,*]

1 Grupo de Materia Condensada-UdeA, Instituto de Física, Facultad de Ciencias Exactas y Naturales, Universidad de Antioquia (UdeA), Cl 70 No. 52-21, Medellín 050010, Colombia; alvaro.morales@udea.edu.co
2 Instituto Tecnológico Metropolitano (ITM)-Institución Universitaria, Calle 73 No. 76A-354 Vía al Volador, Medellín 050034, Colombia; johngil1275@correo.itm.edu.co
3 Departamento de Electrónica y Tecnología de Computadores, Facultad de Ciencias, Universidad de Granada, 18071 Granada, Spain; hahn@ugr.es
4 Centro de Investigación en Ciencias-Instituto de Investigación en Ciencias Básicas y Aplicadas (IICBA), Universidad Autónoma del Estado de Morelos, Av. Universidad 1001, Cuernavaca CP 62209, Morelos, Mexico; memora@uaem.mx
* Correspondence: carlos.dagua@udea.edu.co (C.A.D.-C.); carlos.duque1@udea.edu.co (C.A.D.)

Abstract: External fields modify the confinement potential and electronic structure in a multiple quantum well system, affecting the light–matter interaction. Here, we present a theoretical study of the modulation of the nonlinear optical response simultaneously employing an intense non-resonant laser field and an electric field. Considering four occupied subbands, we focus on a GaAs/AlGaAs symmetric multiple quantum well system with five wells and six barriers. By solving the Schrödinger equation through the finite element method under the effective mass approximation, we determine the electronic structure and the nonlinear optical response using the density matrix formalism. The laser field dresses the confinement potential while the electric field breaks the inversion symmetry. The combined effect of both fields modifies the intersubband transition energies and the overlap of the wave functions. The results obtained demonstrate an active tunability of the nonlinear optical response, opening up the possibility of designing optoelectronic devices with tunable optical properties.

Keywords: GaAs/AlGaAs symmetric multiple quantum well system; intersubband transition energies; electro-optical modulation; nonlinear optical response

check for updates

Received: 2 April 2025
Revised: 17 May 2025
Accepted: 20 May 2025
Published: 12 June 2025

Citation: Dagua-Conda, C.A.; Gil-Corrales, J.A.; Herrero-Hahn, R.V.; Mora-Ramos, M.E.; Morales, A.L.; Duque, C.A. Electro-Optical Modulation of the Nonlinear Optical Response in a GaAs/AlGaAs Symmetric Multiple Quantum Well System. *Physics* **2025**, *7*, 22. https://doi.org/10.3390/physics7020022

1. Introduction

The control of light propagation through semiconductor heterostructures with multiple quantum wells (MQWs) has become a subject of intense research over the past decade [1–9]. In MQW systems, the effective coupling between wells typically arises when the structural parameters of the quantum wells are carefully modified and cause discrete localized energy levels of each well to begin to interact strongly. This interaction leads to extended states that spread over several wells rather than isolated quantized levels [10]. The latter in turn can lead to changes in the band structure that significantly alter the interaction of light with matter, leading to notable nonlinear phenomena reported in experiments, such as high-harmonic generation processes including nonlinear optical rectification (NOR) [11], second-harmonic generation (SHG) [12], and third-harmonic generation (THG) [13], which play a crucial role in modulating the emission spectrum of incident light [14]. In contrast to bulk materials, electronic confinement in MQW systems can be tailored, leading to enhanced nonlinearities [15]. Furthermore, in MQW systems, the possibility of engineering diverse configurations enables tunable nonlinear responses with potential applications in electro-optical modulators [16], far-infrared detectors [17], semiconductor optical amplifiers [18], quantum information theory [19,20], and nonlinear processes such as four-wave mixing [21].

In recent years, two approaches for modifying the nonlinear optical (NLO) properties in semiconductor heterostructures have been studied: the non-resonant intense laser (nIL) field and the electric field [22–27]. The nIL field alters quantum confinement, whereas the electric field breaks the inversion symmetry, enabling precise control over the NLO behavior. Although modifying structural parameters—such as well and barrier widths—in MQW systems has successfully generated enhanced optical nonlinearities, practical applications often require fixed quantum well dimensions. To address this, external fields offer a compelling alternative: they enable tunable control of higher-order harmonic generation while preserving the system's structural configuration. For example, in a combined theoretical and experimental study, Ref. [28] reports the effects of electric fields—both parallel and perpendicular to the quantum well layers—on optical absorption in GaAs/AlGaAs quantum well structures. The results obtained demonstrate that an electric field, whether applied parallel or perpendicular to the quantum well layers, induces significant changes in optical absorption. Reference [29] studies the linear and nonlinear optical properties in a confining potential modeled from the symmetric and asymmetric harmonic-Gaussian potential of double quantum wells under the effect of an applied magnetic field. The findings show that the structural parameters allow control of the coupling between the two wells of the system, and the asymmetry parameter induces changes in the system's selection rules. In addition, introducing a magnetic field produces blue or red shifts in the optical properties of the system. Additionally, Ref. [30] have investigated the effects of a laser field and an electric field, applied in different directions, on the intersubband optical absorption in a graded $Ga_{1-x}Al_xAs/GaAs$ quantum well structure. The results obtained demonstrate that the intersubband transitions depend directly on the applied external fields. Subsequent studies have exploited various approaches to modify the NLO properties, including temperature and pressure effects [31–34], magnetic fields [35], and excitonic effects [36].

It is known that the application of an electric field on a MQW system modifies the confinement potential experienced by the electrons in the system, which can lead to the breaking of the inversion symmetry and, consequently, to an adjustment of the intersubband transition (ISBT) energies and dipole moment matrix elements (DMMEs), which are fundamental factors in the nonlinear optical response of the system [37–39]. For example, the experimental study [40] presented a tunable nonlinear response resulting from the electrical modulation of an intersubband polariton metasurface composed of MQW. Other experimental studies have reported an electro-optical modulation effect of light at low voltages and speeds on the order of MHz in lithium niobate metasurfaces [41], electro-optical modulation in ring resonators [42], and significant second-harmonic generation as a result of a linear electro-optical effect in atomically thin 2D (two-dimensional) materials [43].

However, the nIL field induces a dressing effect on the confinement profile of the MQW system, modifying the effective potential by reducing the depth of the wells and decreasing the height of the barriers. Consequently, particle confinement is altered, leading to a shift in energy levels without changing the original symmetry of the system [44]. Reference [45] demonstrated the effect of the nIL field on the nonlinear optical properties of a Morse quantum well. The findings reveal shifts in the positions of the peaks in both the optical absorption coefficient and the refractive index. Furthermore, other studies indicate that the combined effects of nIL and magnetic fields can modulate the interaction forces between particles and alter the energy level [46]. Various earlier studies on the NLO response in multiple quantum well systems have focused on electrical or optical modulation of the response [5,25]. However, electro-optical modulation has received limited attention, although it is known that effective coupling between wells in MQW structures can induce strong light–matter interactions, significantly enhancing the nonlinear response [47].

Since external fields critically determine the system's nonlinear optical response, the ability to tune both fields independently and simultaneously is highly desirable. For this purpose, we focus on a GaAs/AlGaAs semiconductor heterostructure, because its mature fabrication methods allow precise control over well and barrier thickness and molecular composition [48]. Additionally, these heterostructures possess well-defined energy levels and a tunable bandgap by external fields.

In this paper, we perform flexible control over the ISBT energies and DMMEs by applying the nIL and the electric fields. To this end, we theoretically investigate the effect of external fields on the electronic properties of the MQW system through optical and electrical means Figure 1a. We focus on a GaAs/$Al_{0.3}Ga_{0.7}As$ MQW system, considering four electron subbands. The results obtained demonstrate that combining these external fields enables a unified electro-optical manipulation of the NLO response. Furthermore, we show that the external fields have a measurable impact on the ISBT energies and DMMEs. Finally, we present optimal configurations of the external field values that modulate the transition energy intersections, and the manipulation of the position of the resonant peaks involved in the susceptibility coefficient, which determines the efficiency of light conversion and allows active tunability of the NLO response. While the unified electro-optical scheme applied demonstrates quite a control over the ISBT energies and DMMEs via combined field effects, future studies to extend our model to include nonperturbative time-domain simulations, time-dependent electric field, temperature effects in carrier density, and many-body carrier dynamics to more accurately predict the true dynamic tuning limits and cross-coupled nonlinearities in operational electro-optical modulators.

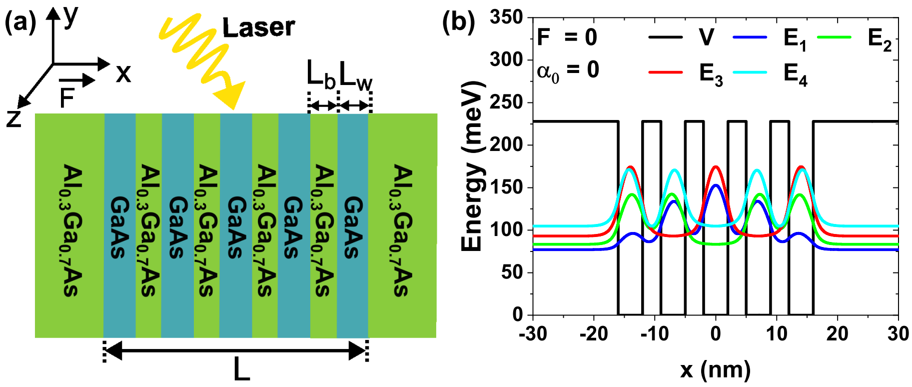

Figure 1. (**a**) Schematic diagram of a GaAs/$Al_{0.3}Ga_{0.7}As$ multiple quantum well system subjected to an external electric field ($\vec{F}$) and a non-resonant intense laser field (α_0). Here, L_w (L_b) denotes the well (barrier) width, and the polarization of the laser field is aligned with the quantum well growth direction. (**b**) The potential profile in the absence of electric field and nIL field (i.e., $F = 0$ and $\alpha_0 = 0$), together with the probability density distributions for the first four subband electrons for the 4 nm wells and 3 nm barriers. E_i, $i = 1, 2, 3,$ and 4, represents the energy of each subband, and V denotes the confinement potential of the structure.

This paper is organized as follows. In Section 2, we present the derivation of the laser-dressed potential energy for a MQW system under the influence of the nIL field and derive the expressions for the coefficients of the NLO response and the DMMEs. Section 3 defines the parameters used in the current study. Section 4 presents the results obtained on the influence and control of the NLO response through external fields. In Section 5, we summarize the findings.

2. Theoretical Framework

In this section, we first outline the dressing effect of the nILF field on the confining potential. Next we detail the derivation of the NLO response using the nonlinear susceptibility coefficients. In addition, we provide the relevant expressions for the DMMEs. We consider a symmetric MQWs system with GaAs ($Al_{0.3}Ga_{0.7}As$) well and barrier regions L_w and L_b widths, respectively. The total length L of the system is the sum of 6 barriers and 5 wells. We calculate the corresponding subband energy levels, density probability, and NLO response, such as the NOR, SHG, and THG, derived from the intersubband transitions of the MQWs under a nIL field and an electric field.

2.1. Laser-Dressed Potential Energy

The time-independent Schrödinger equation in the effective mass approximation, under the effect of an applied external electric field and a non-resonant intense laser field, the confinement potential V changes according to the Kramers–Henneberger transformation as follows [49]:

$$\left[-\frac{\hbar^2}{2}\nabla\cdot\left(\frac{1}{m^*(\vec{r})}\nabla\right)+\langle V(\vec{r},\alpha_0)\rangle-e\vec{F}\cdot\vec{r}\right]\psi(\vec{r})=E\,\psi(\vec{r})\,. \tag{1}$$

where $m^*(\vec{r})$ is the position-dependent electron effective mass, ψ is the wave function, $\hbar$ is the reduced Planck constant, e is the absolute value of electron charge, $\vec{F}$ is the electric field, E is the electron energy eigenvalue, $\langle V(\vec{r},\alpha_0)\rangle$ is the laser-dressed potential of the system, and α_0 is the laser-dressing parameter. The quantum wells are grown along the x-axis, and the external electric field lies along the growth direction, and we assume that the nIL field is polarized in the same direction. The reference frame origin is set at the geometrical center of the heterostructure.

We use the separation of variables method to obtain a 1D differential equation for the x-coordinate. In this approach, the wave function is written in terms of the wave vector $\vec{k}_\perp$ and the electron coordinate $\vec{\lambda}$ in the yz-plane (perpendicular to the growth direction of the heterostructure) $\psi(\vec{r})=e^{i\vec{k}_\perp\cdot\vec{\lambda}}\Psi_n(x)$, where $\Psi_n(x)$ is the eigenfunction of the nth subband. Assuming the bottom of all energy subbands, $\vec{k}_\perp=0$. Therefore, by applying a Fourier expansion to the potential and using Floquet's theory [50], while considering only a high-frequency laser field, one obtains the time-independent Schrödinger equation as follows:

$$\left[-\frac{\hbar^2}{2}\frac{d}{dx}\left(\frac{1}{m^*(x)}\frac{d}{dx}\right)+\langle V(x,\alpha_0)\rangle-eF(x-L/2)\right]\Psi_n(x)=E_n\Psi_n(x)\,, \tag{2}$$

where E_n is the electron energy eigenvalue associated with the eigenfunction $\Psi_n(x)$ and F is the electric field strength. A shift of $-L/2$ is introduced in the x-coordinate to set the zero of the potential energy at that point of the structure. The second term of Equation (2) accounts for the laser-dressed potential and reads:

$$\langle V(x,\alpha_0)\rangle=\frac{\omega'}{2\pi}\int_0^{2\pi/\omega'}V\big[x+\alpha_0\sin(\omega' t)\big]\,dt\,. \tag{3}$$

In Equation (3), the explicit form of the term associated with a classical displacement of the electron under the influence of an electric field is replaced: $\vec{\alpha}(t)=\alpha_0\sin(\omega' t)\hat{x}$ with

ω' the non-resonant frequency, $\hat{x}$ indicating the propagation direction of the field and $\alpha_0 \equiv eA_0/(m^*(x)\omega'^2)$, where A_0 the field strength [44].

The intensity of the nIL field is determined by the laser-dressing parameter α_0, which can be defined in terms of the time-averaged intensity $I = \frac{1}{2}|A_0|^2\epsilon_0 c$ of the laser field as [18]:

$$I = \frac{\alpha_0^2\,\omega'^4\,m_{\text{eff}}^{*2}\,\epsilon_0\,c}{2\,e^2}\,, \tag{4}$$

where c denotes the speed of light and ϵ_0 is the permittivity of the vacuum. Following a procedure similar to that of Ref. [51]:

(i) We choose a specific amplitude in the high-intensity regime of the laser field (i.e., the laser-dressing parameter) $\alpha_0 = 4\,\text{nm}$.

(ii) For the GaAs/AlGaAs heterostructure under use, the characteristic intensity at high (above 215 THz) frequencies is defined by $I_c = m_{\text{eff}}^{*2}\,\alpha_B^{*2}\,\omega^4\,c\,\epsilon_0\,\epsilon_r^{1/2}/(2\,e^2)$ [52], where $\alpha_B^* = \hbar^2\,\epsilon_r/(m_{\text{eff}}^*\,k\,e^2) = 1.4\,\text{nm}$ is the effective Bohr radius, $\omega/2\pi = 100$ THz is the laser frequency, $\epsilon_r = 10.89$ is the relative dielectric constant at high frequencies, and k is the Coulomb constant.

(iii) To deal with the problem of non-uniform effective masses, we use only in this part of the study, the mean harmonic average effective mass approximation [53]:

$$\frac{1}{m_{\text{eff}}^*} = \frac{L_w}{L}\,\frac{1}{m_w^*} + \frac{L_b}{L}\,\frac{1}{m_b^*}\,, \tag{5}$$

where m_w^* and m_b^* represent the effective mass corresponding to GaAs wells and AlGaAs barriers. Equation (5) provides us with an approximate value of the electron effective mass. However, in what follows, to account for the effect of external fields on the superlattice, we used the position-dependent electron effective mass $m^*(x)$.Thus, one obtains an approximate value of the characteristic intensity at high frequencies, which is $I_c \approx 7.3 \times 10^{11}$ W/cm^2.

(iv) Using Equation (4) for $\alpha_0 = 4\,\text{nm}$, we calculate a maximum intensity value, $I_{\text{max}} = 1.8 \times 10^{12}\,\text{W/cm}^2$. Although the maximum value of the intensity exceeds the characteristic intensity at high frequencies, typically the intensities of about $10^{12}\,\text{W/cm}^2$ are accepted in experimental procedures [54,55].

Finally, we solve the differential equation corresponding to the Schrödinger Equation (2) using the finite element method (FEM) implemented in the COMSOL Multiphysics semiconductor module, which discretizes across interface-specific partial differential equations (PDEs) using a Galerkin weighted-residual formulation with user-controlled adaptive mesh refinement [56]. After the energy levels and corresponding wave functions are determined, we compute the NLO properties and the relative shifts in the ISBT energies and DMMEs.

2.2. Nonlinear Optical Response

To study the NLO response, we employ a semi-classical approach. This method combines a quantum description of the interacting particle with a classical representation of the radiation field. The radiation field is modeled as monochromatic optical radiation, characterized by the electric field $E(t)$, which is polarized along the growth direction of the quantum wells, i.e.,

$$E(t) = E_0 e^{i\omega t} + \text{c.c.}\,, \tag{6}$$

where E_0 is the complex amplitude and 'c.c.' stands for complex conjugate. Using the density matrix formalism and assuming a phenomenological approach to the dissipative process, the Liouville–von Neumann equation explicitly describes the dissipative process time evolution via the following master equation [57]:

$$\frac{\partial \rho_{ij}}{\partial t} = \frac{1}{i\hbar}\left[\hat{H}_0 + \hat{H}_I, \hat{\rho}\right]_{ij} - \Gamma_{ij}\left(\hat{\rho} - \hat{\rho}^{(0)}\right)_{ij}, \tag{7}$$

where $\hat{\rho}$ is the density matrix operator, $\hat{M}$ is the dipole moment operator and Γ_{ij} are the matrix terms of the phenomenological operator $\hat{\Gamma}$. The steady-state density matrix $\hat{\rho}^{(0)}$ is diagonal and its elements $\rho_{ii}^{(0)}$ represent the electron populations of the ith energy levels E_i. $\hat{H}_0 = \sum_{k=1}^{4} \hbar\omega_k |k\rangle\langle k|$ is the free Hamiltonian of the system in the absence of the electric field for the four subbands, and $\hat{H}_I = -\hat{M}E(t) = -e\hat{x}E(t)$ is the perturbation term that accounts for the light–matter interaction. The phenomenological operator $\hat{\Gamma}$ incorporates damping effects caused by interactions between electrons and phonons and electron–electron collisions. We assume that $\hat{\Gamma}$ is a diagonal matrix associated with the relaxation process and its elements are the inverse of the relaxation time that involves the $|m\rangle$ state, $\Gamma_{mm} = 1/\tau_m$, $m = 1, 2,$ and 3 [58], for brevity noted as Γ_m in what follows.

The master Equation (7) is solved using a perturbative method, in which the system is divided into an unperturbed part $\hat{H}_0$ and a perturbative part $\hat{H}_I$ that introduces negligibly small corrections to the system dynamics. This approach yields a series of solutions, each perturbative order adding corrections to the total evolution. Consequently, the density matrix is expanded perturbatively in terms of the electric field as:

$$\hat{\rho}(t) = \sum_{n=0}^{\infty} \hat{\rho}^{(n)}(t), \tag{8}$$

where $\hat{\rho}^{(n)}$ is the n-th perturbative order of the density matrix. Replacing into the Equation (7) and using the completeness relation $\sum_k |k\rangle\langle k| = \mathbb{1}$, one has:

$$\begin{aligned}\frac{\partial \rho_{ij}^{(n+1)}}{\partial t} = \frac{1}{i\hbar}\sum_{n=0}^{\infty}\Bigg[\sum_{k=1}^{4}\Big\{&\hbar\,\omega_k\Big(\delta'_{ik}\,\rho_{kj}^{(n+1)} - \delta'_{kj}\,\rho_{ik}^{(n+1)}\Big)\\ &- E(t)\Big(M_{ik}\,\rho_{kj}^{(n)} - M_{kj}\,\rho_{ik}^{(n)}\Big)\Big\} - i\hbar\,\Gamma_{ij}\,\rho_{ij}^{(n+1)}\Bigg].\end{aligned} \tag{9}$$

Here δ' is the Kronecker delta. The different perturbative orders of ρ can be expanded as follows:

$$\frac{\partial \rho_{ij}^{(1)}}{\partial t} = \frac{1}{i\hbar}\sum_{k=1}^{4}\Big\{\hbar\,\omega_k\Big(\delta'_{ik}\,\rho_{kj}^{(1)} - \delta'_{kj}\,\rho_{ik}^{(1)}\Big) - E(t)\Big(M_{ik}\,\rho_{kj}^{(0)} - M_{kj}\,\rho_{ik}^{(0)}\Big)\Big\} - i\hbar\,\Gamma_{ij}\,\rho_{ij}^{(1)}, \tag{10}$$

$$\frac{\partial \rho_{ij}^{(2)}}{\partial t} = \frac{1}{i\hbar}\sum_{k=1}^{4}\Big\{\hbar\,\omega_k\Big(\delta'_{ik}\,\rho_{kj}^{(2)} - \delta'_{kj}\,\rho_{ik}^{(2)}\Big) - E(t)\Big(M_{ik}\,\rho_{kj}^{(1)} - M_{kj}\,\rho_{ik}^{(1)}\Big)\Big\} - i\hbar\,\Gamma_{ij}\,\rho_{ij}^{(2)}, \tag{11}$$

$$\frac{\partial \rho_{ij}^{(3)}}{\partial t} = \frac{1}{i\hbar}\sum_{k=1}^{4}\Big\{\hbar\,\omega_k\Big(\delta'_{ik}\,\rho_{kj}^{(3)} - \delta'_{kj}\,\rho_{ik}^{(3)}\Big) - E(t)\Big(M_{ik}\,\rho_{kj}^{(2)} - M_{kj}\,\rho_{ik}^{(2)}\Big)\Big\} - i\hbar\,\Gamma_{ij}\,\rho_{ij}^{(3)}. \tag{12}$$

We assume, in the weak probe approximation, that the all-electron population at $t = 0$ is in the ground state, which requires $\rho_{11}^{(0)} = 1$, $\rho_{22}^{(0)} = \rho_{33}^{(0)} = \rho_{44}^{(0)} = 0$ and $\rho_{ij}^{(0)} = 0$ for $i \neq j$. The analytical solution for the matrix elements at different perturbative orders is obtained using a procedure similar to that from Refs. [57,58].

The electronic polarization and susceptibility coefficients are related through the light polarization degree, induced by the electric field $E(t)$. This relation is derived by equating terms proportional to $\exp(\pm\omega_n t)$ in the polarization expansion with those obtained from the perturbative expansion of the density matrix in the steady-state response

$\hat{\rho}^{(n)}(t) = \tilde{\rho}^{(n)}(\omega)e^{-i\omega_n t} + \tilde{\rho}^{(n)}(-\omega)e^{i\omega_n t}$ with $\omega_n = \{0, \omega, 2\omega, 3\omega\}$, through the following equation [59]:

$$\begin{aligned}\hat{P}^{(n)}(t) =& \frac{1}{V}\,\mathrm{tr}\left\{\hat{\rho}^{(n)}\hat{M}\right\} \\ =& \epsilon_0\left(\chi_\omega^{(1)}\tilde{E}e^{-i\omega t} + \chi_0^{(2)}\tilde{E}^2 + \chi_{2\omega}^{(2)}\tilde{E}^2 e^{-2i\omega t} + \chi_\omega^{(3)}\tilde{E}^2\tilde{E}e^{-i\omega t} + \chi_{3\omega}^{(3)}\tilde{E}^3 e^{-3i\omega t} + \text{c.c.}\right),\end{aligned} \tag{13}$$

where 'tr' denotes the trace operation, V is the volume of the system, and $\chi_\omega^{(1)}, \chi_0^{(2)}, \chi_{2\omega}^{(2)}, \chi_\omega^{(3)}$ and $\chi_{3\omega}^{(3)}$ are the linear optical susceptibility, nonlinear optical rectification, second-harmonic generation, third order linear susceptibility and third-harmonic generation, respectively. The current study focuses on the coefficients associated with optical rectification, second-harmonic generation, and third-harmonic generation.

Finally, the corresponding expressions per unit surface read:

$$\chi_0^{(2)} = \frac{4e^3\sigma_V}{\epsilon_0}M_{21}^2\delta_{21} \times \frac{E_{21}^2(1+\Gamma_2/\Gamma_1) + \hbar^2(\omega^2+\Gamma_2^2)(\Gamma_2/\Gamma_1 - 1)}{\left((E_{21}-\hbar\omega)^2 + (\hbar\Gamma_2)^2\right)\left((E_{21}+\hbar\omega)^2 + (\hbar\Gamma_2)^2\right)}, \tag{14}$$

$$\chi_{2\omega}^{(2)} = \frac{e^3\sigma_V}{\epsilon_0} \times \frac{M_{21}M_{32}M_{31}}{(\hbar\omega - E_{21} - i\hbar\Gamma_3)(2\hbar\omega - E_{31} - i\hbar\Gamma_3/2)}, \tag{15}$$

$$\chi_{3\omega}^{(3)} = \frac{e^4\sigma_V}{\epsilon_0} \times \frac{M_{21}M_{32}M_{43}M_{41}}{(\hbar\omega - E_{21} - i\hbar\Gamma_3)(2\hbar\omega - E_{31} - i\hbar\Gamma_3/2)(3\hbar\omega - E_{41} - i\hbar\Gamma_3/3)}, \tag{16}$$

where $E_{ij} = E_i - E_j$ is the intersubband transition energy, and σ_V is the carrier density. In Equations (14)–(16), the DMMEs are defined as:

$$M_{fi} = \int \Psi_f^*(x)x\Psi_i(x)dx \quad (i, f = 1, 2, 3, 4), \tag{17}$$

where $\delta_{21} = |M_{22} - M_{11}|$, M_{ij} (M_{ii}) are the off-diagonal (on-diagonal) DMMEs, and the eigenfunctions $\Psi_i(x)$ and $\Psi_f(x)$ to be obtained from Equation (2).

3. System and Parameters

The system consists of a sequence of five coupled GaAs quantum wells and six $Al_xGa_{1-x}As$ barriers, as illustrated in Figure 1b. Due to quite small separation between the subbands, close to the longitudinal optical (LO) phonon energies ($\hbar\omega_{LO} \approx 36$ meV in GaAs), this structure exhibits short excited states lifetimes ($\tau \approx 1$ ps) [60]. This short lifetime of electrons in the excited subbands primarily arises from electron-phonon interactions, the dominant mechanism for energy relaxation in this system.

For the calculations, the following parameters were used from the measurements: an Al concentration of $x = 0.3$, based on the 60%:40% distribution rule for the band offset between the conduction and valence bands, respectively. The barrier height is expressed as $V_0 = \Xi(E_g^{\mathrm{AlGaAs}} - E_g^{\mathrm{GaAs}}) = 228$ meV, where E_g denotes the band gap energy, $\Xi = 0.60$ [61]. We consider the well (barrier) width of 4 nm (3 nm). The effective electron mass for GaAs (AlGaAs) is $m_w^* = 0.067\,m_0$ ($m_b^* = 0.09\,m_0$), $\sigma_V = 4 \times 10^{20}\,1/\mathrm{m}^3$, $\Gamma_1 = 1/(2\,\mathrm{ps})$, $\Gamma_2 = 1/(1.5\,\mathrm{ps})$, and $\Gamma_3 = 1/(1.0\,\mathrm{ps})$ [13,59,62].

4. Results and Discussion

In this Section, we discuss the external field-mediated electro-optical control of the ISBT energies and the DMMEs. To proceed systematically, we first analyze the influence of individual fields (electric and nIL) separately, followed by their combined effect. Next we consider the cases where the ISBT energies and wavefunction overlap are manipulated using purely electrical or optical means. Finally, we delve into the impact of simultaneous electric and laser fields on the NLO response of the MQWs system.

4.1. Influence of the External Fields on the DMMEs and the ISBT Energies

Figure 1b shows the profile of the conduction band for a $GaAs/Al_{0.3}Ga_{0.7}As$ symmetric MQW system composed of five wells and six barriers. The probability density associated with the first four states is also depicted, corresponding to the eigenenergies E_1 to E_4. Without any external field ($F = 0$ and $\alpha_0 = 0$), the initial symmetric confinement potential profile results in alternating symmetric and antisymmetric parity for the wave functions. The electrons in the ground state are located to a greater extent at the central quantum well center (see the blue curve), with the probability density being maximum at this point and different from zero in all the wells, which indicates that there may be tunneling of the electrons. The maximum probability density is located in the central well because the electrons favor regions of minimal confinement, which is in agreement with theoretical expectations.

Figure 2 shows the modifications to the potential due to the presence of the nIL field and the electric field. Figure 2a shows the potential modified by a nIL field without an electric field ($F = 0$, black line) and the first four probability densities of the confined states. In the presence of the nIL field, a new symmetric potential arises in the system of wells and barriers, which directly depends on the changes in the laser-dressing parameter α_0, as shown in the figure (compare Figure 1b with Figure 2a). For $\alpha_0 = 4\,\text{nm}$, the number of wells is modified in the system, going from five to four effective wells; note that in the initial system, at the center position ($x = 0$), there was one well and the laser effect transforms this well into a barrier. In addition, all wells become shallower and wider at the top and narrower at the bottom, leading to a noticeable separation in energy levels. This behavior has also been earlier reported in Ref. [63] for values of the laser parameter larger than the well width $\alpha_0 > L/2$. As a result, the electrons are distributed mainly in the two central wells (blue curve).

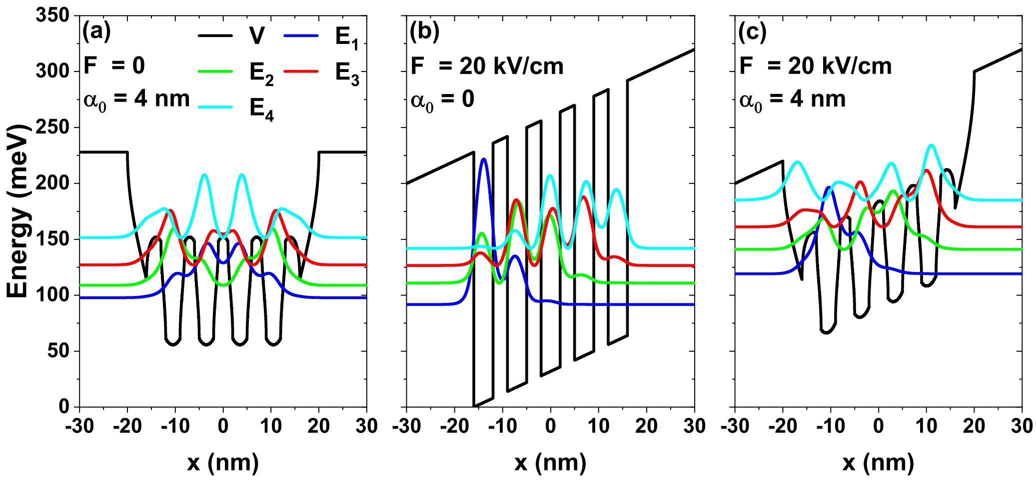

Figure 2. Change in the confinement potential for two distinct scenarios for modifications induced by the external fields for the $GaAs/Al_{0.3}Ga_{0.7}As$ multiple quantum well system with 4 nm wells and 3 nm barriers when (**a**) the non-resonant intense laser field dressed the potential, altering the width and height of barriers and wells and (**b**) the electric field tilts the potential and shifts the charge distribution, and (**c**) due to the combined effect of a fixed non-resonant intense laser field of $\alpha_0 = 4\,\text{nm}$ and a fixed value of the electric field strength of $F = 20\,\text{kV/cm}$.

Figure 2b shows the potential profile modified by the effects of the electric field without the nIL field ($\alpha_0 = 0$) and its corresponding probability densities. The electric field induces polarization in the system, tilts the potential, and shifts the charge distribution, breaking the inversion symmetry of the system. Due to this, the electrons experience a force that displaces them parallel to the fields and locates them in the wells on the left. Figure 2c shows the potential in the presence of both fields, the nIL ($\alpha_0 = 4\,\mathrm{nm}$) and the electric field ($F = 20\,\mathrm{kV/cm}$). We observe a combined effect in the modified potential: alterations in the shapes of the wells and barriers caused by the nIL field and a tilt induced by the electric field. Note that, with the action of both fields, the MQW system undergoes a significant change in the electron confinement, which may alter its electronic and optical properties.

Figures 3 shows the ISBT energies between the first four states as a function of the laser-dressing parameter and the electric field strength for the symmetric GaAs/$Al_{0.3}Ga_{0.7}As$ MQW system illustrated in Figure 1. Note that the ISBT energies are scaled (that is, divided by a factor of two and three: $E_{31}/2$ and $E_{41}/3$, respectively), which is a direct consequence of the quantization of energy levels in confined semiconductor structures. This scaling facilitates the analysis of the optical properties discussed later in this investigation. The curves include the first four states as functions of the aforementioned external fields, which allows for a direct observation of the ISBT energy modification induced. Figure 3a,d show the ISBT energies as a function of the electric field. Without the nIL field (Figure 3a), a monotonic increase in the behavior of the ISBT energies is observed with increasing electric field strength (see Table 1). Furthermore, three ISBT energy intersections occur: $E_{21} = E_{31}/2$, $E_{21} = E_{41}/3$ and $E_{41} = 3E_{31}/2$, in the electric field range $F \approx 7.5$–$12.5\,\mathrm{kV/cm}$, these factors come from the denominators of Equations (15) and (16) to obtain a maximum in the corresponding susceptibilities. The intersections result from the coincidence between the ISBT energies in a specific range of electric field values. This coincidence influences the dynamics of the system's optical response. Intersections of the ISBT energies play an important role in improving the efficiency of nonlinear optical processes because they allow the simultaneous fulfillment of multiple resonance conditions. By tuning the quantum system (e.g., with an electric field or a non-resonant intense laser field) to operate near an intersection point where $E_{21} \approx E_{31}/2$, multiple energy denominators in the nonlinear susceptibility expression Equation (15) become quite small. Significant dipole moments of the ISBT energies also dramatically enhance the nonlinear optical response and a significantly higher conversion efficiency for processes such as SHG and THG, as shown in this work. These results are fundamental in designing highly efficient nonlinear optical devices based on quantum wells and other nanostructures.

The insets in Figure 3 show that the energies do not present crossings or anticrossings. In contrast to Figure 3a, in Figure 3c the $E_{21} = E_{31}/2$ and $E_{21} = E_{41}/3$ intersections are observed, in this case for an electric field value of $F \approx 15\,\mathrm{kV/cm}$, instead of the $F \approx 7\,\mathrm{kV/cm}$ of Figure 3a This shift towards higher energy values arises because of the modifications in the potential profile induced by the nIL field. Figure 3b shows the ISBT energies as a function of the laser-dressing parameter without an electric field. The increase in the laser-dressing parameter induces a monotonic increasing behavior of the ISBT energies without intersections between them. In contrast, the application of an electric field, Figure 3d, is again responsible for the occurrence of intersections between the ISBT energy pairs: $E_{31} = 2, E_{31}/3$ and $E_{21} = E_{41}/3$, for values of the laser-dressing parameter $\alpha_0 \approx 2.5$–$4\,\mathrm{nm}$.

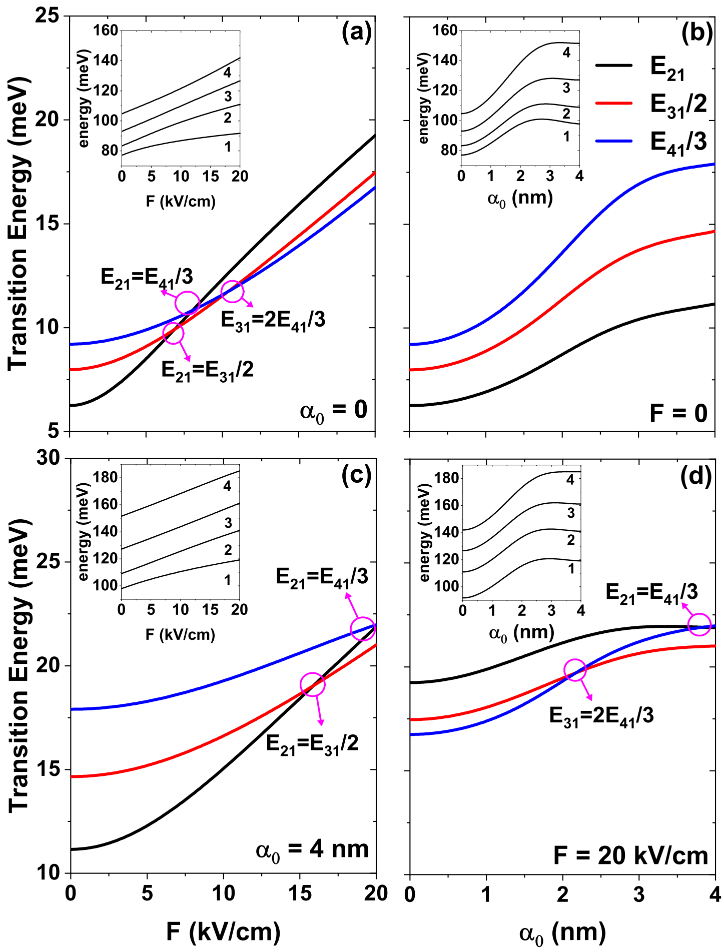

Figure 3. The intersubband transition energy $E_{ij} = E_i - E_j$ as a function of the electric field strength (**a**,**c**) and of the laser-dressing parameter α_0 (**b**,**d**) for the GaAs/$Al_{0.3}Ga_{0.7}As$ multiple quantum well system with 4 nm wells and 3 nm barriers due to the manipulating the intersubband transition energies by purely electrical and optical means (**a**,**b**) and to the combined effect of the external fields on the intersubband transition energies (**c**,**d**) for (**c**) a fixed non-resonant intense laser field of $\alpha_0 = 4$ nm and (**d**) a fixed value of the electric field strength of $F = 20$ kV/cm. Insets show the energy eigenvalue associated with the first four subbands. Pink circles indicate the intersection between intersubband transition energies.

Table 1. Exact values of the intersubband transition energy $E_{ij} = E_i - E_j$ for varying electric field strength F and the laser-dressing parameter α_0.

α_0 (nm)	F (kV/cm)	E_{21} (meV)	$E_{31}/2$ (meV)	$E_{41}/3$ (meV)
0	0	6.25	7.89	9.21
	5	8.50	9.09	9.89
	10	12.33	11.53	11.58
	20	19.25	17.46	16.75
4	0	11.15	14.66	17.91
	5	12.29	15.19	18.28
	10	15.05	16.62	19.27
	20	21.88	21.01	21.97

Considering the effects of external fields on the ISBT energies, we can now explore the manipulation of the DMMEs through these fields. The DMMEs as a function of the electric field strength without a nIL field ($\alpha_0 = 0$) and with a nIL field ($\alpha_0 = 4$) are shown in Figure 4a and Figure 4c, respectively. In Figure 4a, without the nIL field, a monotonic decrease is observed in the matrix elements $|M_{21}|$, $|M_{32}|$, $|M_{41}|$, and $|M_{43}|$ as the strength of the electric field increases. For $|M_{31}|$ and $|M_{22} - M_{11}|$, a non-zero value is obtained, due to the breaking of the symmetry inversion induced by the electric field, which enables transitions that while considered forbidden. With increasing electric field strength, the wave functions shift and deform, reaching at some point an optimal overlap ($F \approx 10\,\text{kV/cm}$) that maximizes the DMMEs $|M_{31}|$ and $|M_{22} - M_{11}|$. For higher field values, distortion and excessive shifting reduce the overlap, causing the matrix elements to decrease again. In contrast, the DMMEs $|M_{21}|$, $|M_{32}|$, $|M_{41}|$, and $|M_{43}|$ show a monotonic decrease as the electric field strength increases, suggesting a lower overlap of the wave functions. In Figure 4c, the nIL field causes the matrix elements $|M_{21}|$ and $|M_{32}|$ to decrease just slightly as the electric field increases (compared to Figure 4a). For the DMMEs involving the fourth state ($|M_{41}|$ and $|M_{43}|$), a non-monotonic behavior is appreciable because this state, for high nIL field strengths ($\alpha_0 = 4\,\text{nm}$), can be coupled with the continuum states (cyan line in Figure 2c). Furthermore, the maximum value of the matrix elements $|M_{31}|$ and $|M_{22} - M_{11}|$ shifts towards higher values of the electric field ($F \approx 15\,\text{kV/cm}$) and remains almost constant from that value onward. All this suggests that the nIL field alters the overlapping wave functions and shifts the values of the electric field where maxima occur in the DMMEs.

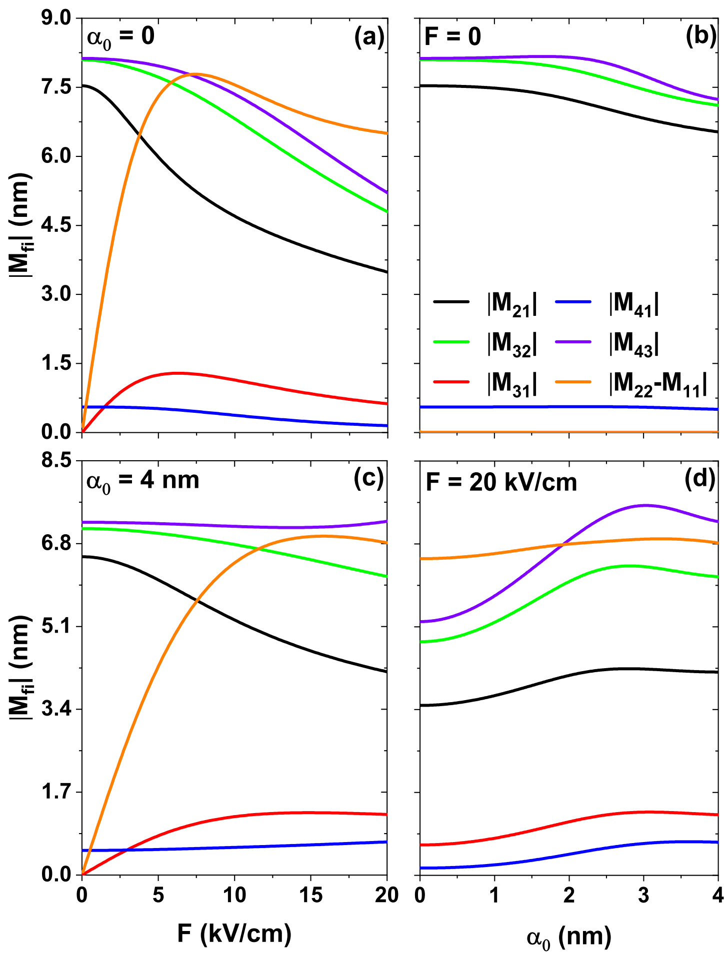

Figure 4. The dipole moment matrix elements as a function of the electric field strength (**a**,**c**) and of the laser-dressing parameter α_0 (**b**,**d**) for the $GaAs/Al_{0.3}Ga_{0.7}As$ multiple quantum well system with 4 nm wells and 3 nm barriers due to the manipulating the intersubband transition energies by purely electrical and optical means (**a**,**b**) and the combined effect of the external fields on the dipole moment matrix elements (**c**,**d**) for (**c**) a fixed nIL field of $\alpha_0 = 4\,\text{nm}$ and (**d**) a fixed value of the electric field of $F = 20\,\text{kV/cm}$.

Figure 4b,d show the DMMEs as a function of the laser-dressing parameter, without an electric field ($F = 0$) and with an electric field ($F = 20\,\mathrm{kV/cm}$), respectively. In Figure 4b, with $F = 0$, a slight decrease of the matrix elements $|M_{21}|, |M_{32}|, |M_{41}|$, and $|M_{43}|$ is observed as the nIL field increases. Furthermore, $|M_{31}|$ and $|M_{22} - M_{11}|$ remain constant at zero (the associated lines are superimposed on the plot), indicating that the nIL field slightly alters the overlapping of the wave functions and does not break the inversion symmetry, preserving its initial selection rules. In Figure 4d, the electric field $F = 20\,\mathrm{kV/cm}$ breaks the inversion symmetry of the system and the DMMEs increase as a function of the laser-dressing parameter, reaching a maximum value for $\alpha_0 \approx 3\,\mathrm{nm}$, and slightly decreasing from that value onward. The reason behind this is the displacement and overlapping of the wave functions produced by the effects of both fields.

Before calculating the susceptibility coefficients, it is convenient to study how these external fields alter the NLO response in the system. These changes are, in principle, associated with the so-called geometric factors, which refer to the terms involving the product between the DMMEs in each susceptibility coefficient. Figure 5a,b show the geometric factor $M_{21}^2\delta_{21}$, where $\delta_{21} = |M_{22} - M_{11}|$, associated with the nonlinear optical rectification NOR Equation (14), as a function of the electric field strength and the laser-dressing parameter, respectively. In Figure 5a, without the nIL field (solid line), it is observed that the geometric factor reaches its maximum value for an electric field of $F \approx 5\,\mathrm{kV/cm}$, decreasing from this point onward as the field increases (see Table 2). With an nIL field of $\alpha_0 = 4\,\mathrm{nm}$ (dashed line), the maximum value shifts to higher field intensities and is reached for an electric field of $F \approx 7.5\,\mathrm{kV/cm}$. The reason for this lies in the non-monotonic variation of the DMMEs M_{21}^2 and δ_{21} with the electric field, and their product reaches a maximum value in the ranges where both are relatively large (see Figure 4a). Figure 5b shows that, in the absence of an electric field (solid line), the geometric factor remains zero when varying the laser-dressing parameter because the nIL field does not break the inversion symmetry of the system so that the term δ_{21} involving the matrix elements M_{11} and M_{22} is zero (see Figure 4b). In contrast, in the presence of an electric field (dashed line), a non-monotonic behavior is observed in the curve associated with the geometric factor, reaching its maximum value for a nIL field of $\alpha_0 \approx 3\,\mathrm{nm}$.

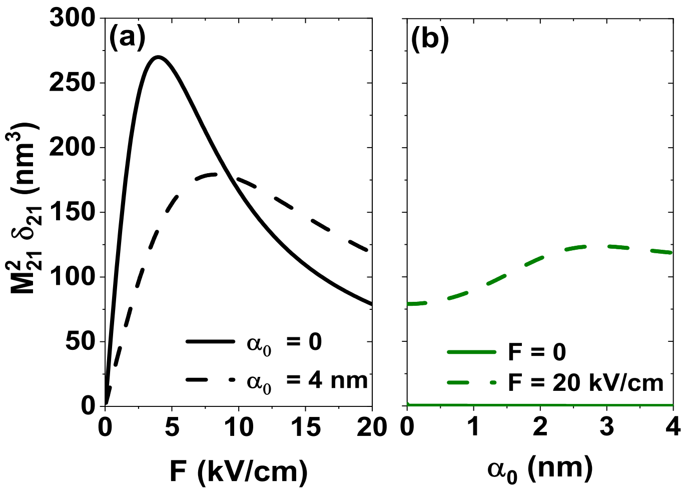

Figure 5. The geometrical factor $M_{21}^2\delta_{21}$ as a function the electric field strength F (**a**) and of the laser-dressing parameter α_0 (**b**). The dashed line shows the combined electric and non-resonant intense laser field effect, while the solid line shows a single-field effect. See text for details.

Table 2. Exact values of the geometrical factors for the varying electric field strength F and the laser-dressing parameter α_0. See text for details.

α_0 (nm)	F (kV/cm)	$M_{21}^2\delta_{21}$ (nm^3)	$M_{21}M_{32}M_{31}$ (nm^3)	$M_{21}M_{32}M_{43}M_{41}$ (nm^4)
0	0	1.57	0.44	275.10
	5	261.58	57.80	191.47
	10	166.83	36.55	88.53
	20	78.94	10.45	12.98
4	0	0.04	0.01	169.66
	5	156.83	34.187	160.64
	10	175.44	42.52	144.02
	20	118.59	31.75	125.89

Figure 6 shows the geometric factor $M_{21}M_{32}M_{31}$, associated with the SHG Equation (15), as a function of the electric field strength and the laser-dressing parameter. In Figure 6a, in the absence of the nIL field (solid line), it is observed that the geometric factor reaches its maximum value for an electric field of $F \approx 5\,\mathrm{kV/cm}$. Meantime, when an nIL field is applied to the system (dashed line), a reduction is observed for the maximum values, in addition to a shift towards an electric field value of $F \approx 10\,\mathrm{kV/cm}$. Figure 6b shows that in the absence of an electric field, the geometric factor remains constant at zero by varying the laser-dressing parameter because the matrix element M_{31} requires the inversion symmetry breaking induced by the electric field (see Figure 4b).

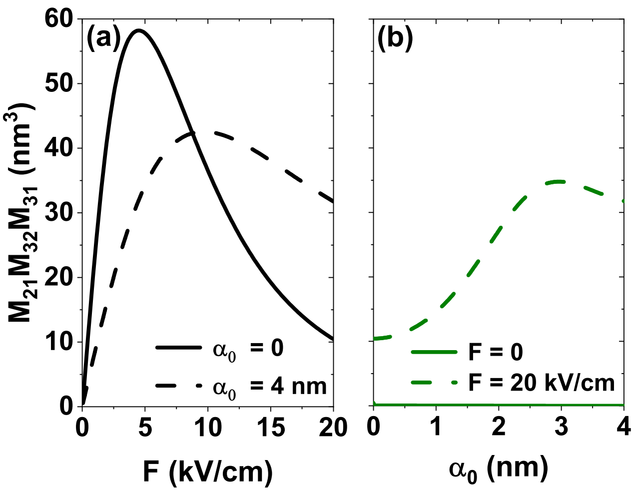

Figure 6. The geometrical factor $M_{21}M_{32}M_{31}$ as a function of the electric field strength F (**a**) and of the laser-dressing parameter α_0 (**b**). The dashed line shows the combined electric and non-resonant intense laser field effect, and the solid line shows a single-field effect.

Figure 7 shows the geometric factor $M_{21}M_{32}M_{43}M_{41}$, associated with third-harmonic generation (THG) Equation (16), as a function of the electric field strength and the laser-dressing parameter. In comparison to the geometric factors discussed just above for Figure 6, the geometric factor shown in Figure 7 does not require the electric-field-induced inversion symmetry breaking, due to the alternating symmetry and antisymmetric parity of the wavefunctions; therefore, the matrix elements involved are non-zero as a function of the external fields, as shown in Figure 4. In Figure 7a, the geometric factor exhibits a monotonic decrease as the intensity of the electric field increases, in both the absence of the nIL field (solid line) and the presence of nIL field (dashed line). The main difference lies in the maximum values reached at $F = 0$ by the factor in the presence of the nIL field, while without this field, the maximum value of the factor becomes lower, with a better pronounced decrease as the electric field strength increases. Figure 7b shows the curves of the geometric factor as a function of the nIL field. In the absence of an electric field (solid line), the factor remains nearly constant for a laser-dressing parameter α_0 ranging from 0 to about 1 nm. For larger parameter values of the laser-dressing parameter, the geometric factor decreases monotonically. When an electric field of $F = 20\,\mathrm{kV/cm}$ is applied, the opposite behavior is observed, that is, the geometric factor increases monotonically for $\alpha_0 > 1\,\mathrm{nm}$, which is rather constant for lower values.

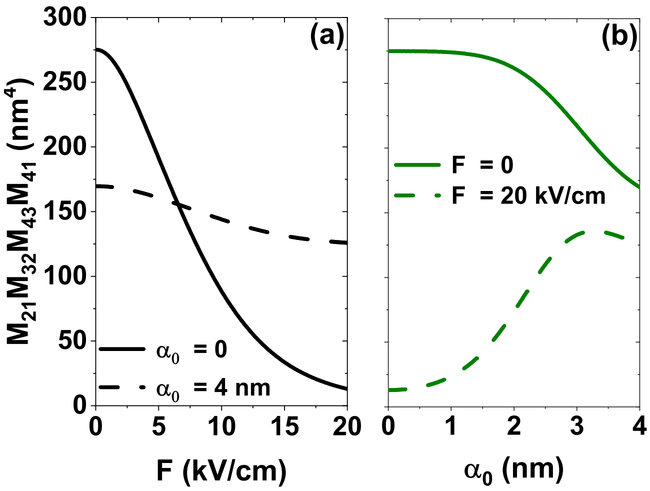

Figure 7. The geometrical factor $M_{21}M_{32}M_{43}M_{41}$ as a function of the electric field strength F (**a**) and of the laser-dressing parameter α_0 (**b**). The dashed line shows the combined electric and non-resonant intense laser field effect, and the solid line shows a single-field effect.

4.2. External Fields Control Nonlinear Optical Response

Figure 8 shows the NOR coefficient $\chi_0^{(2)}$ (14) as a function of the incident photon energy for different values of the electric field strength and the nIL field. Figure 8a shows that in the absence of the nIL field ($\alpha_0 = 0$), the peak associated with the NOR coefficient reaches its maximum value when $F = 5\,\mathrm{kV/cm}$. As the electric field increases, this peak experiences a blueshift, and its maximum value decreases. The energy shift is due to the energy of the intersubband transition E_{21}, involved in the NOR coefficient, which exhibits a monotonic increase (black line in Figure 3a). The findings indicate that the increase in the electric field generates a separation between the intersubband levels, shifting the resonance peak towards higher energies. Additionally, the decrease in the maximum value occurs because the electric field alters the shape and position of the quantum state wave functions, thereby modifying their overlap. This effect is illustrated by the solid line in Figure 5a, which shows that the geometric factor reaches a maximum value at approximately $F = 5\,\mathrm{kV/cm}$ before decreasing as the field increases. Finally, it is to be stressed that for $F = 0$, the NOR peak is zero since the electric field is required to generate the nonlinear response of the system.

To highlight how the nIL field alters the NOR response, we compare to the zero nIL case Figure 8a by showing in Figure 8b the NOR coefficient versus incident photon energy for the same four electric field strengths when $\alpha_0 = 4\,\mathrm{nm}$. The immediate conclusion one can make, while comparing Figure 8b to Figure 8a, is that the magnitude of the maximum value reached by the NOR coefficient for $F = 5\,\mathrm{kV/cm}$ is lower in the presence of the nIL field than that in the absence of the nIL. In Figure 8b when $F = 10\,\mathrm{kV/cm}$, the NOR peak exhibits a blueshift and its intensity reaches a maximum; however, for fields beyond $10\,\mathrm{kV/cm}$, the intensity decreases. This blueshift happens because that, under the influence of the nIL field, the geometric factor associated with the NOR (see Figure 5a, dashed line) experiences a shift in its maximum value and a decrease in its magnitude. Finally, Figure 8c presents the NOR peak as a function of the photon energy for different values of the laser-dressing parameter α_0 in the presence of an electric field of $F = 20\,\text{kV/cm}$. In contrast to Figure 8a,b, here the blueshift of the peak is less pronounced and its magnitude increases as α_0 grows. The confinement induced by the nIL field produces a slight blueshift in the E_{21} intersubband energy as α_0 increases (black line in Figure 3d), influencing, therefore, on the separation between levels, which turns into a less marked shift toward higher energies. As discussed just above for Figure 8b, the curve associated with the geometric factor (Figure 5b, dashed line) determines the behavior of the NOR peak maximum value. The combined effect of the electric field and the nIL field offers a tunable mechanism that modifies both the energy level separation and the overlap of the wave functions. These variations dynamically tune the magnitude and spectral position of the nonlinear optical rectification.

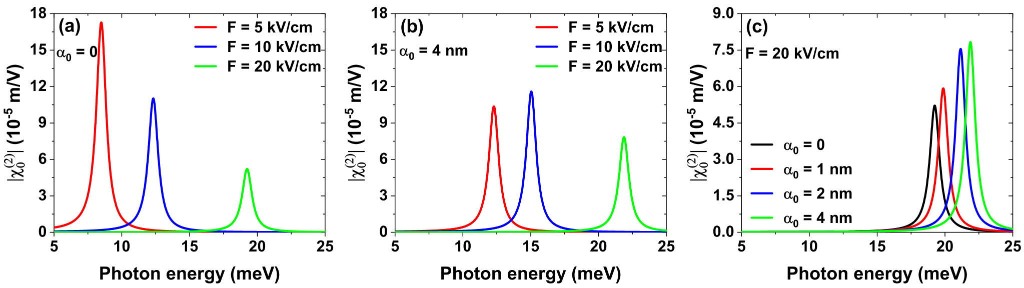

Figure 8. The nonlinear optical rectification coefficient $\chi_0^{(2)}$ (14) as a function of the incident photon energy for (**a**,**b**) different values of the electric field strength F with zero, $\alpha_0 = 0$ (**a**), and non-zero, $\alpha_0 = 4$ (**b**), non-resonant intense laser field, and for (**c**) different values of the non-resonant intense laser field parameter at a fixed electric field of $F = 20\,\text{kV/cm}$.

Figure 9 shows the SHG coefficient $\chi_{2\omega}^{(2)}$ (15) as a function of the incident photon energy for different values of the electric field and the nIL field. In Figure 9a, when $\alpha_0 = 0$ (absence of the nIL field), the SHG coefficient exhibits a blueshift with the photon energy, and when the coefficient reaches its maximum value ($F = 7\,\text{kV/cm}$, pink curve) the magnitude decreases as the intensity of the electric field increases. This blueshift happens due to the monotonic increase of the intersubband transition energies E_{21} and E_{31} with the electric field strength (see Figure 3a, black and red curves). Furthermore, one observes that at $F = 7\,\text{kV/cm}$, the two characteristic peaks of the SHG coefficient are merged into a single peak with the highest magnitude; however, as the electric field strength increases, the peaks move apart. This separation influences the maximum value of the SHG coefficient that describes the efficiency of the process and depends on both the intersubband transition energies and the incident photon energy. In contrast to Figure 8, the maximum value of the SHG coefficient is not governed exclusively by the behavior of the geometric factor $M_{21}M_{32}M_{31}$ but depends mainly on the approach or intersections between the ISBT energies. As the peaks are moved apart, the energies E_{21} and E_{31} become more distinguishable, indicating a change in the electronic structure of the multiple quantum well system induced by the electric field. This phenomenon is straightforwardly shown from the variations in the level spacing (see Figure 3a, black and red curves): at $F = 5\,\text{kV/cm}$, the transition energies are close (even crossing $E_{21} = E_{31}/2$ at $F = 7\,\text{kV/cm}$, pink circle Figure 3a), as the electric field strength increases, the peaks start moving apart. The moving apart of the peaks reduces the efficiency of SHG since the mismatch between resonances prevents the incident photon energy from being transferred efficiently, producing a notable decrease in the maximum coefficient value. Nevertheless, as the peaks move apart, SHG becomes more selective concerning the photon incident frequencies, implying that the system responds strongly only at specific frequencies corresponding to the individual ISBT energies.

In Figure 9b, the presence of the nIL field ($\alpha_0 = 4\,\mathrm{nm}$) causes a blueshift and an increase in the magnitude of the SHG coefficient as the electric field strength increases, reaching its maximum value at $F = 16\,\mathrm{kV/cm}$ (pink curve), from this point on, the coefficient decreases. The blueshift is associated with increased ISBT energies with the electric field strength (see Figure 3c). However, in contrast to Figure 9a, the two characteristic peaks of the SHG coefficient are initially separated and closer as the electric field strength increases. When an approach or intersection occurs between the intersubband transition energies E_{21} and E_{31} ($F = 16\,\mathrm{kV/cm}$, see Figure 3c pink circle), the two characteristic peaks of the SHG coefficient merge into a single but more intense peak. This indicates that the incident photon energy coincides, at some point, with the intersection between the ISBT energies, what maximizes the SHG efficiency under this resonance condition. In this scenario, the incident photon energy is transferred more effectively to the second-harmonic generation process. The induced coincidence, through the two external fields, between the ISBT energies involved in the SHG leads to a significant increase in the magnitude of the second-harmonic signal. Finally, Figure 9c shows that under a fixed electric field of $F = 20\,\mathrm{kV/cm}$, both a blueshift and an increase in the maximum value of the SHG coefficient occur as the laser-dressing parameter increases. Initially, the characteristic peaks of the SHG coefficient are separated. However, as the laser-dressing parameter increases, these peaks become closer. In this case, the ISBT energies E_{21} and E_{31} do not cross (see Figure 3d) at $\alpha_0 = 4\,\mathrm{nm}$ the highest magnitude of the SHG coefficient is observed.

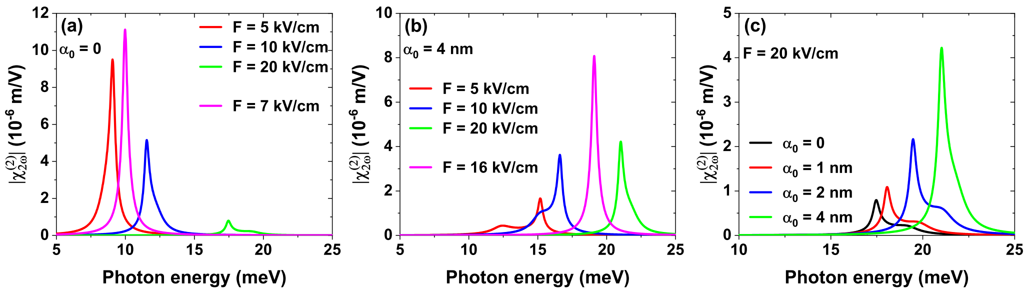

Figure 9. The second harmonic generation coefficient $\chi^{(2)}_{2\omega}$ (15) as a function of the incident photon energy for (**a**,**b**) different values of the electric field strength F at zero, $\alpha_0 = 0$ (**a**), and non-zero, $\alpha_0 = 4\,\mathrm{nm}$ (**b**), non-resonant intense laser field, and (**c**) at different values of the non-resonant intense laser field parameter and a fixed electric field of $F = 20\,\mathrm{kV/cm}$. The pink curve (**a**,**b**) shows the second-harmonic generation coefficient when $E_{21} = E_{31}/2$.

Figure 10a and Figure 10b show the THG coefficient $\chi^{(3)}_{3\omega}$ (16) as a function of the incident photon energy for different values of the electric field strength in the absence ($\alpha_0 = 0$) and presence ($\alpha_0 = 4\,\mathrm{nm}$) of the nIL field, respectively. In Figure 10a, for electric field intensities ranging in 0–10 kV/cm, the THG coefficient shows a blueshift with a coalescence of the three characteristic peaks and an increase in magnitude. The coefficient for $F = 20\,\mathrm{kV/cm}$ breaks the observed trend and undergoes a notable decrease in magnitude and a splitting of the peaks. The blueshift occurs due to the monotonic increase in the ISBT energies E_{21}, E_{31}, and E_{41} (see Figure 3a). The three peaks are attributed to the findings from Figure 3a that, in the range of $F \approx 7.5$–$12.5\,\mathrm{kV/cm}$, these transition energies approach each other considerably (even presenting intersections between pairs such as $E_{21} = E_{31}/2$, $E_{21} = E_{41}/3$ and $E_{31} = 2E_{41}/3$ but no coincidence between the three energies in a single point is found), while for $F > 12.5\,\mathrm{kV/cm}$ E_{31} and E_{41} remain close and E_{21} separates, originating the appearance of two peaks close together and one further away. As discussed above for Figure 7a, the behavior of the geometric factor $M_{21}M_{32}M_{43}M_{41}$ as a function of F (see Figure 7a, dashed line) does not explain the maximum values reached by the THG coefficient, what are mainly related to proximity and intersections between the ISBT energies. In particular, the maximum value observed for the THG coefficient at $F = 10\,\mathrm{kV/cm}$ indicates that for this specific electric field value, the ISBT energies E_{21}, E_{31} and E_{41} (Figure 3a) are closer one to another what favors the efficiency of the THG process. Whereas for $F = 20\,\mathrm{kV/cm}$, the separation of the peaks reduces the magnitude of the THG coefficient and confers selectivity concerning the incident photon frequencies. Compared to Figure 10a, in Figure 10b, the presence of the nIL field causes the characteristic THG peaks to initially be more separated, preserving the blueshift discussed above, but causing the appearance of the maximum value at $F = 20\,\mathrm{kV/cm}$. These results indicate that, by applying the nIL field, it is possible to adjust the electric field values at which approaches or intersections occur between ISBT energies and, in this way, determine the optimal combination of external fields that improves the THG efficiency. The results obtained also demonstrate that the efficiency of the THG process can be improved when external fields induce coincidences between the ISBT energies. Moreover, external fields can also separate the ISBT energies and make the THG process highly selective with incident photon frequencies.

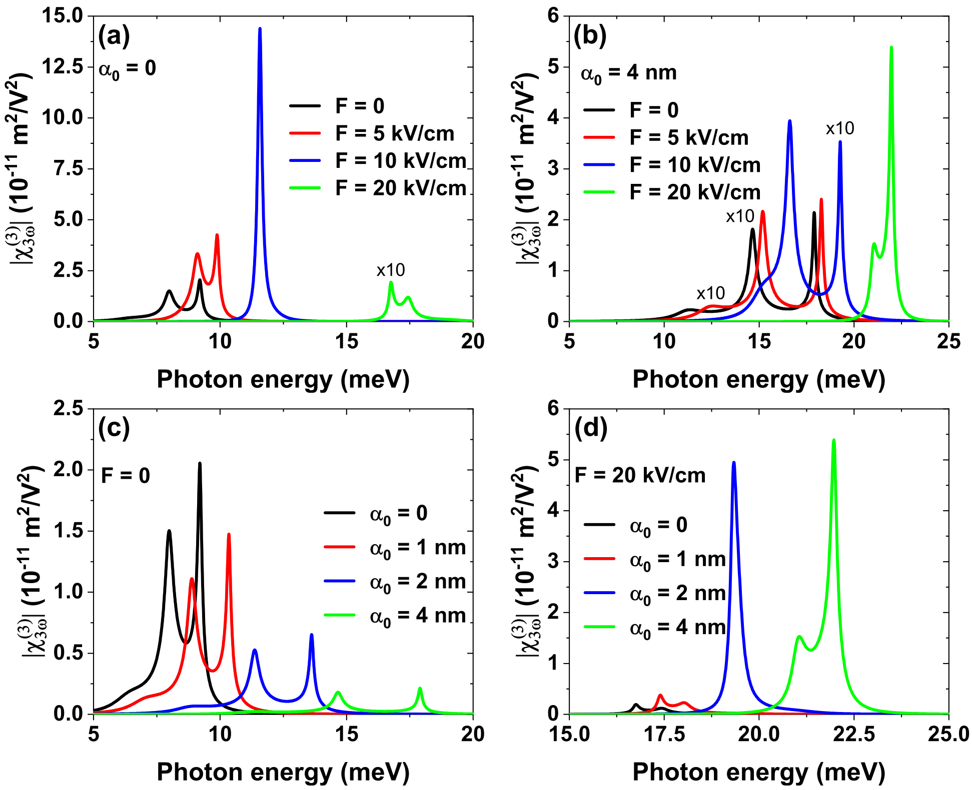

Figure 10. The third harmonic generation coefficient $\chi^{(3)}_{3\omega}$ (16) as a function of the incident photon energy for (**a**,**b**) different values of the electric field strength F at zero non-resonant intense laser field $\alpha_0 = 0$ (**a**) and at $\alpha_0 = 4\,\mathrm{nm}$ (**b**), and (**c**,**d**) for different values of the non-resonant intense laser field α_0 without electric field $F = 0$ (**c**) and applying an electric field of $F = 20\,\mathrm{kV/cm}$ (**d**). A factor of 10 is applied to some third-harmonic generation coefficient curves to for better visibility.

Figure 10c and Figure 10d show the THG coefficient as a function of the incident photon energy for different values of the laser-dressing parameter in the absence ($F = 0$) and presence ($F = 20\,\mathrm{kV/cm}$) of the electric field, respectively. In Figure 10c, as the nIL field increases, a blueshift is observed to occur being accompanied by a progressive separation of the three characteristic peaks and a decrease in their magnitude. This blueshift is attributed to the monotonic increase of the ISBT energies E_{21}, E_{31}, and E_{41} as a function of the nIL field (see Figure 3c). The separation of the peaks significantly influences the magnitude of the THG coefficient, suggesting that, in the multiple quantum well system, increasing the nIL field reduces the THG efficiency, although it improves the selectivity concerning the incident photon frequencies. The observed behaviour may be of use in applications that require selective interaction with specific frequencies. On the other hand, Figure 10d shows that, in the presence of an electric field, the THG coefficient undergoes a weaker blueshift and its magnitude increases considerably as the nIL field increases. This small enough shift is due to the slight growth of the ISBT energies with the nIL field (see Figure 3d). For an electric field of $F = 20\,\mathrm{kV/cm}$, the THG coefficient's characteristic peaks align with the ISBT energies' dependence on the laser-dressing parameter. From Figure 3d, one observes that E_{31} and E_{41} are quite close one to another, while E_{21} is separated what resuts in two closely spaced peaks and one well-defined peak in Figure 10d. This trend persists until the laser-dressing parameter reaches approximately 1.5 nm, while beyond this value, an intersection occurs between the energies E_{31} and $2E_{41}/3$ (Figure 3d), causing the two adjacent peaks to merge into a single peak. However, the peak corresponding to E_{21} remains isolated. Notably, under these conditions, the magnitude of the THG coefficient increases substantially (see blue curve). A similar effect emerges for $\alpha_0 = 4\,\mathrm{nm}$ (see Figure 10b), where another intersection arises between E_{21} and $E_{41}/3$ (Figure 3c). All three ISBT energies converge at this point ($\alpha_0 = 4\,\mathrm{nm}$), leading to a higher enhancement in the magnitude of the THG coefficient.

5. Conclusions

In this paper we theoretically investigate the modulation of the nonlinear optical response in a $GaAs/Al_{0.3}Ga_{0.7}As$ symmetric multiple quantum well system under the simultaneous application of an IL field and an electric field. We find that the nIL field modifies the electron confinement potential without altering the initial symmetry of the system; the so-induced changes affect the overlap of the wave functions and the electronic structure, leading to variations in the spacing between subbands and, consequently, in the ISBT energies. Meantime, the electric field is found to tilt the confinement potential. This alters the electronic distribution, breaking the inversion symmetry, and enabling transitions between states while considered forbidden by the selection rules. In addition, the electronic field is found to modify, similarly to the nIL field, both the wave functions' overlap and the separation between subbands.

To analyze the nonlinear optical response, we determine the impact of each field on the ISBT energies and the wave function overlap, quantified by the geometrical factor. The results show that the simultaneous application of both external fields enables the manipulation of both the overlap of the wave functions and the coupling or intersection between the ISBT energies, which are determining factors in the nonlinear optical response of the system. The behavior of the geometrical factor as a function of the nIL field and the electric field is shown to determine the efficiency of the nonlinear optical rectification; then the system reaches a high efficiency when this factor reaches its maximum value. Additionally, accidental intersections, induced by external fields, between pairs of ISBT energies is found to improve the efficiency in the second and third-harmonic generation. Instead, the ISBT energy separation confers selectivity to the system concerning the frequencies of the incident photon. The results indicate the possibility of tuning the wavefunction overlap and ISBT energies by applying both external fields, demonstrating an active tunability of the nonlinear optical response in the multi-quantum well system. The findings might be employed in the design of optoelectronic devices with tunable optical properties.

Author Contributions: Conceptualization, C.A.D.-C. and J.A.G.-C.; methodology, C.A.D.-C. and J.A.G.-C.; formal analysis, C.A.D.-C., J.A.G.-C., R.V.H.-H., A.L.M., M.E.M.-R. and C.A.D.; investigation, C.A.D.-C., J.A.G.-C., R.V.H.-H. and A.L.M.; writing—original draft, C.A.D.-C.; writing—review

& editing, C.A.D.-C., R.V.H.-H., M.E.M.-R. and C.A.D.; software, C.A.D.-C. and J.A.G.-C.; supervision, A.L.M. All authors have read and agreed to the published version of the manuscript.

Funding: The authors would like to thank to the Colombian Agencies: Comité para el Desarrollo de la Investigación (CODI) -Universidad de Antioquia (Estrategia de Sostenibilidad de la Universidad de Antioquia and projects "Complejos excitónicos y propiedades de transporte en sistemas nanométricos de semiconductores con simetría axial basados en GaAs e InAs", and "Nanoestructuras semiconductoras con simetría axial basadas en InAs y GaAs para aplicaciones en electrónica ultra e híper rápida") and Facultad de Ciencias Exactas y Naturales-Universidad de Antioquia (C.A.D. exclusive dedication project 2025–2026). R.V.H.-H. gratefully acknowledges financial support from the Spanish Junta de Andalucía through a Doctoral Training Grant PREDOC-01408.

Data Availability Statement: No new data were created or analyzed in this study. Data sharing is not applicable to this article.

Conflicts of Interest: The authors declare no conflicts of interest.

References

1. Solaimani, M.; Morteza, I.; Arabshahi, H.; Reza, S.M. Study of optical nonlinear properties of a constant total effective length multiple quantum wells system. *J. Lumin.* **2013**, *134*, 699–705. [CrossRef]
2. Yesilgul, U.; Ungan, F.; Kasapoglu, E; Sari, H.; Sökmen, I. Linear and nonlinear optical properties in asymmetric double semi-V-shaped quantum well. *Phys. B Condens. Matter* **2015**, *475*, 110–116. [CrossRef]
3. Zhao, Q.; Aqiqi, S.; You, J.-F.; Kria, M.; Guo, K.-X.; Feddi, E.; Zhang, Z.-H.; Yuan, J.-H. Influence of position-dependent effective mass on the nonlinear optical properties in $\mathrm{Al}_x\mathrm{Ga}_{1-x}\mathrm{As/GaAs}$ single and double triangular quantum wells. *Phys. E Low- Dimens. Syst. Nanostruct.* **2020**, *115*, 113707. [CrossRef]
4. Hien, N.D. Linear and nonlinear optical properties in quantum wells. *Micro Nanostruct.* **2022**, *170*, 207372. [CrossRef]
5. Altun, D.; Ozturk, O.; Alaydin, B.O.; Ozturk, E. Linear and nonlinear optical properties of a superlattice with periodically increased well width under electric and magnetic fields. *Micro Nanostruct.* **2022**, *166*, 207225. [CrossRef]
6. Mukherjee, R.; Hazra, R.; Borgohain, N. Controlling behavior of transparency and absorption in three-coupled multiple quantum wells via spontaneously generated coherence. *Sci. Rep.* **2024**, *14*, 8197. [CrossRef]
7. Gil-Corrales, J.A.; Morales, A.L.; Behiye Yücel, M.; Kasapoglu, E.; Duque, C.A. Electronic transport properties in GaAs/AlGaAs and InSe/InP finite superlattices under the effect of a non-resonant intense laser field and considering geometric modifications. *Int. J. Mol. Sci.* **2022**, *23*, 5169. [CrossRef]
8. Rodríguez-Magdaleno, K.A.; Demir, M.; Ungan, F.; Nava-Maldonado, F.M.; Martínez-Orozco, J.C. Third harmonic generation of a 12–6 $\mathrm{GaAs/Ga}_{1-x}\mathrm{Al}_x\mathrm{As}$ double quantum well: Effect of external fields. *Eur. Phys. J. Plus* **2024**, *139*, 359. [CrossRef]
9. Kasapoglu, E.; Sari, H.; Sökmen, I.; Vinasco, J.A.; Laroze, D.; Duque, C.A. Effects of intense laser field and position dependent effective mass in Razavy quantum wells and quantum dots. *Phys. E Low-Dimens. Syst. Nanostruct.* **2021**, *126*, 114461. [CrossRef]
10. Tuzemen, A.T.; Dakhlaoui, H.; Mora-Ramos, M.E.; Ungan, F. The nonlinear optical properties of GaAs/GaAlAs triple quantum well: Role of the electromagnetic fields and structural parameters. *Phys. B Condens. Matter* **2022**, *646*, 414286. [CrossRef]
11. Rosencher, E.; Bois, P.; Nagle, J.; Costard, E.; Delaitre, S. Observation of nonlinear optical rectification at 10.6 μm in compositionally asymmetrical AlGaAs multiquantum wells. *Appl. Phys. Lett.* **1989**, *55*, 1597–1599. [CrossRef]
12. D'Andrea, A.; Tomassini, N.; Ferrari, L.; Righini, M.; Selci, S.; Bruni, M.R.; Schiumarini, D.; Simeone, M.G. Second harmonic generation in stepped InAsGaAs/GaAs quantum wells. *Phys. Status Solidi A* **1997**, *164*, 383–386. [CrossRef]
13. Sirtori, C.; Capasso, F.; Sivco, D.L.; Cho, A.Y. Giant, triply resonant, third-order nonlinear susceptibility $\chi^{(3)}_{3\omega}$ in coupled quantum wells. *Phys. Rev. Lett.* **1992**, *68*, 1010–1013. [CrossRef]
14. Ido, T.; Tanaka, S.; Suzuki, M.; Koizumi, M.; Sano, H.; Inoue, H. Ultra-high-speed multiple-quantum-well electro-absorption optical modulators with integrated waveguides. *J. Lightwave Technol.* **1996**, *14*, 2026–2034. [CrossRef]
15. Gil-Corrales, J.A.; Dagua-Conda, C.A.; Mora-Ramos, M.E.; Morales, A.L.; Duque, C.A. Shape and size effects on electronic thermodynamics in nanoscopic quantum dots. *Phys. E Low-Dimens. Syst. Nanostruct.* **2025**, *170*, 116228. [CrossRef]
16. Miyazeki, Y.; Yokohashi, H.; Kodama, S.; Murata, H.; Arakawa, T. InGaAs/InAlAs multiple-quantum-well optical modulator integrated with a planar antenna for a millimeter-wave radio-over-fiber system. *Opt. Express* **2020**, *28*, 11583–11596. [CrossRef]
17. Heshmati, M.M.K.; Emami, F. Optimized design and simulation of optical section in electro-reflective modulators based on photonic crystals integrated with multi-quantum-well structures. *Optics* **2023**, *4*, 227–245. [CrossRef]
18. Dutta, N.K.; Wang, Q. *Semiconductor Optical Amplifiers*; World Scientific: Singapore, 2006. [CrossRef]
19. Carrillo, R.S.; Gil-Barrera, C.A.; Sun, G.H.; Solaimani, M.; Dong, S.H. Shannon entropies of asymmetric multiple quantum well systems with a constant total length. *Eur. Phys. J. Plus.* **2021**, *136*, 1060. [CrossRef]

20. Carrillo, R.S.; Dong, Q.; Sun, G.H.; Silva-Ortigoza, R.; Dong, S.H. Shannon entropy of asymmetric rectangular multiple well with unequal width barrier. *Results Phys.* **2022**, *33*, 105109. [CrossRef]
21. Panchadhyayee, P.; Dutta, B.K. Spatially structured multi-wave-mixing induced nonlinear absorption and gain in a semiconductor quantum well. *Sci. Rep.* **2022**, *12*, 22369. [CrossRef]
22. Mora-Ramos, M.E.; Duque, C.A.; Kasapoglu, E.; Sari, H.; Sökmen, I. Electron-related nonlinearities in GaAs–$Ga_{1-x}Al_xAs$ double quantum wells under the effects of intense laser field and applied electric field. *J. Lumin.* **2013**, *135*, 301–311. [CrossRef]
23. Restrepo, R.L.; González-Pereira, J.P.; Kasapoglu, E.; Morales, A.L.; Duque, C.A. Linear and nonlinear optical properties in the terahertz regime for multiple-step quantum wells under intense laser field: Electric and magnetic field effects. *Opt. Mater.* **2018**, *86*, 590–599. [CrossRef]
24. Bahar, M.K.; Rodríguez-Magdaleno, K.A.; Martinez-Orozco, J.C.; Mora-Ramos, M.E.; Ungan, F. Optical properties of a triple AlGaAs/GaAs quantum well purported for quantum cascade laser active region. *Mater. Today Commun.* **2021**, *26*, 101936. [CrossRef]
25. Ozturk, O.; Alaydin, B.O.; Altun, D.; Ozturk, E. Intense laser field effect on the nonlinear optical properties of triple quantum wells consisting of parabolic and inverse-parabolic quantum wells. *Laser Phys.* **2022**, *32*, 035404. [CrossRef]
26. Alaydin, B.O.; Altun, D.; Ozturk, O.; Ozturk, E. High harmonic generations triggered by the intense laser field in GaAs/$Al_xGa_{1-x}As$ honeycomb quantum well wires. *Mater. Today Phys.* **2023**, *38*, 101232. [CrossRef]
27. Solaimani, M.; Dong, S.-H. Optical rectification and effective equivalence between the asymmetric multiple quantum well and electric field potentials for fixed total length GaAs/AlGaAs systems. *Solid State Commun.* **2025**, *397*, 115813. [CrossRef]
28. Miller, D.A.; Chemla, D.S.; Damen, T.C.; Gossard, A.C.; Wiegmann, W.; Wood, T.H.; Burrus, C.A. Electric field dependence of optical absorption near the band gap of quantum-well structures. *Phys. Rev. B* **1985**, *32*, 1043. [CrossRef]
29. Kasapoglu, E.; Yücel, M.B.; Duque, C.A. Harmonic-gaussian symmetric and asymmetric double quantum wells: Magnetic field effects. *Nanomaterials* **2023**, *13*, 892. [CrossRef]
30. Ozturk, E.; Sari, H.; Sokmen, I. Electric field and intense laser field effects on the intersubband optical absorption in a graded quantum well. *J. Phys. D Appl. Phys.* **2005**, *38*, 935. [CrossRef]
31. Ungan, F.; Yesilgul, U.; Sakiroglu, S.; Mora-Ramos, M.E.; Duque, C.A.; Kasapoglu, E.; Sari, H.; Sökmen, I. Simultaneous effects of hydrostatic pressure and temperature on the nonlinear optical properties in a parabolic quantum well under the intense laser field. *Opt. Commun.* **2013**, *309*, 158–162. [CrossRef]
32. Ungan, F.; Restrepo, R.L.; Mora-Ramos, M.E.; Morales, A.L.; Duque, C.A. Intersubband optical absorption coefficients and refractive index changes in a graded quantum well under intense laser field: effects of hydrostatic pressure, temperature and electric field. *Phys. B Condens. Matter* **2014**, *434*, 26–31. [CrossRef]
33. Ed-Dahmouny, A.; Sali, A.; Es-Sbai, N.; Arraoui, R.; Jaouane, M.; Fakkahi, A.; El-Bakkari, K.; Duque, C.A. Combined effects of hydrostatic pressure and electric field on the donor binding energy, polarizability, and photoionization cross-section in double GaAs/$Ga_{1-x}Al_xAs$ quantum dots. *Eur. Phys. J. B* **2022**, *95*, 136. [CrossRef]
34. Barseghyan, M.G.; Hakimyfard, A.; López, S.Y.; Duque, C.A.; Kirakosyan, A.A. Simultaneous effects of hydrostatic pressure and temperature on donor binding energy and photoionization cross section in Pöschl–Teller quantum well. *Phys. E Low-Dimens. Syst. Nanostruct.* **2010**, *42*, 1618-1622. [CrossRef]
35. Yesilgul, U.; Al, E.B.; Martínez-Orozco, J.C.; Restrepo, R.L.; Mora-Ramos, M.E.; Duque, C.A.; Ungan, F.; Kasapoglu, E. Linear and nonlinear optical properties in an asymmetric double quantum well under intense laser field: Effects of applied electric and magnetic fields. *Opt. Mater.* **2016**, *58*, 107–112. [CrossRef]
36. Mo, S.; Guo, K.; Liu, G.; He, X.; Lan, J.; Zhou, Z. Exciton effect on the linear and nonlinear optical absorption coefficients and refractive index changes in Morse quantum wells with an external electric field. *Thin Solid Films* **2020**, *710*, 138286. [CrossRef]
37. Aqiqi, S.; Duque, C.A.; Radu, A.; Gil-Corrales, J.A.; Morales, A.L.; Vinasco, J.A.; Laroze, D. Optical properties and conductivity of biased GaAs quantum dots. *Phys. E Low-Dimens. Syst. Nanostruct.* **2022**, *138*, 115084. [CrossRef]
38. Walrod, D.; Auyang, S.Y.; Wolff, P.A.; Sugimoto, M. Observation of third order optical nonlinearity due to intersubband transitions in AlGaAs/GaAs superlattices. *Appl. Phys. Lett.* **1991**, *59*, 2932–2934. [CrossRef]
39. Dagua-Conda, C.A.; Gil-Corrales, J.A.; Hahn, R.V.H.; Restrepo, R.L.; Mora-Ramos, M.E.; Morales, A.L.; Duque, C.A. Tuning electromagnetically induced transparency in a double GaAs/AlGaAs quantum well with modulated doping. *Crystals* **2025**, *15*, 248. [CrossRef]
40. Park, S.; Yu, J.; Boehm, G.; Belkin, M.A.; Lee, J. Electrically tunable third-harmonic generation using intersubband polaritonic metasurfaces. *Light Sci. Appl.* **2024**, *13*, 169. [CrossRef]
41. Weigand, H.; Vogler-Neuling, V.V.; Escalé, M.R.; Pohl, D.; Richter, F.U.; Karvounis, A.; Timpu, F.; Grange, R. Enhanced electro-optic modulation in resonant metasurfaces of lithium niobate. *ACS Photonics* **2021**, *8*, 3004–3009. [CrossRef]
42. Hahn, R.V.H.; Duque, C.A.; Mora-Ramos, M.E. Electron-impurity states in concentric double quantum rings and related optical properties. *Phys. Lett. A* **2025**, *534*, 130226. [CrossRef]

43. Chen, Z.; Fang, Y.; Cheng, M.; Lü, T.Y.; Cao, X.; Zhu, Z.Z.; Wu, S. Large second-harmonic generation and linear electro-optic effect in the bulk kagome lattice compound Nb_3MX_7 (M= Se, S, Te; X= I, Br). *Phys. Rev. B* **2024**, *109*, 115118. [CrossRef]
44. Lima, F.M.S.; Amato, M.A.; Olavo, L.S.F.; Nunes, O.A.C.; Fonseca, A.L.A.; da Silva, E.F., Jr. Intense laser field effects on the binding energy of impurities in semiconductors. *Phys. Rev. B* **2007**, *75*, 073201. [CrossRef]
45. Sakiroglu, S.; Kasapoglu, E.; Restrepo, R.L.; Duque, C.A.; Sökmen, I. Intense laser field-induced nonlinear optical properties of Morse quantum well. *Phys. Status Solidi B* **2017**, *254*, 1600457. [CrossRef]
46. Wang, W.; Van Duppen, B.; Van der Donck, M.; Peeters, F.M. Magnetopolaron effect on shallow-impurity states in the presence of magnetic and intense terahertz laser fields in the Faraday configuration. *Phys. Rev. B* **2018**, *97*, 064108. [CrossRef]
47. Li, X.; Wang, X.; Li, Y.; Qin, F.; Jiang, Y.; Wang, L.; Wang, Y. AlInGaAs MQW transceiver with electro-optic modulation characteristics for free-Space optical communication and sensing. *ACS Omega* **2021**, *6*, 23614–23620. [CrossRef]
48. Ladugin, M.A.; Yarotskaya, I.V.; Bagaev, T.A.; Telegin, K.Y.; Andreev, A.Y.; Zasavitskii, I.I.; Padalitsa, A.A.; Marmalyuk, A.A. Advanced AlGaAs/GaAs heterostructures grown by MOVPE. *Crystals* **2019**, *9*, 305. [CrossRef]
49. Henneberger, W.C. Perturbation method for atoms in intense light beams. *Phys. Rev. Lett.* **1968**, *21*, 838–840. [CrossRef]
50. Gavrila, M.; Kamiński, J.Z. Free-free transitions in intense high-frequency laser fields. *Phys. Rev. Lett.* **1984**, *52*, 613–616. [CrossRef]
51. Li, X.; Wang, W.; Zhao, N.; Yang, H.; Han, S.; Liu, W.; Wang, H.; Qu, F.; Hao, N.; Fu, J.; et al. Intense high-frequency laser-field control of spin-orbit coupling in GaInAs/AlInAs quantum wells: A laser dressing effect. *Phys. Rev. B* **2022**, *106*, 155420. [CrossRef]
52. Fanyao, Q.; Fonseca, A.L.A.; Nunes, O.A.C. Hydrogenic impurities in a quantum well wire in intense, high-frequency laser fields. *Phys. Rev. B* **1996**, *54*, 16405–16408. [CrossRef] [PubMed]
53. Gibbs, Z.M.; Ricci, F.; Li, G.; Zhu, H.; Persson, K.; Ceder, G.; Hautier, G.; Jain, A.; Snyder, G.J. Effective mass and Fermi surface complexity factor from ab initio band structure calculations. *npj Comput. Mater.* **2017**, *3*, 8. [CrossRef]
54. Dörr, M.; Potvliege, R.M.; Proulx, D.; Shakeshaft, R. Multiphoton processes in an intense laser field. V. The high-frequency regime. *Phys. Rev. A* **1991**, *43*, 3729–3740. [CrossRef]
55. Di Piazza, A.; Müller, C.; Hatsagortsyan, K.Z.; Keitel, C.H. Extremely high-intensity laser interactions with fundamental quantum systems. *Rev. Mod. Phys.* **2012**, *84*, 1177–1228. [CrossRef]
56. *COMSOL Multiphysics. Version 6.1*; COMSOL AB: Stockholm, Sweden, 2022. Available online: https://www.comsol.com/product-download/6.1 (accessed on 19 May 2025).
57. Boyd, R.W.; Gaeta, A.L.; Giese, E. Nonlinear optics. In *Springer Handbook of Atomic, Molecular*; Drake, G.W.F., Ed.; Springer Springer Nature: Cham, Switzerland, 2023; pp. 1097–1100. [CrossRef]
58. Ahn, D.; Chuang, S.L. Calculation of linear and nonlinear intersubband optical absorptions in a quantum well model with an applied electric field. *IEEE J. Quantum Electron.* **1987**, *54*, 2196–2204.
59. Rosencher, E.; Bois, P. Model system for optical nonlinearities: asymmetric quantum wells. *Phys. Rev. B* **1991**, *44*, 11315. [CrossRef]
60. Sirtori, C.; Nagle, J. Quantum Cascade Lasers: The quantum technology for semiconductor lasers in the mid-far-infrared. *Comptes Rendus Phys.* **2003**, *4*, 639–648. [CrossRef]
61. Adachi, S. *Properties of Semiconductor Alloys: Group-IV, III-V and II-VI Semiconductors*; John Wiley & Sons Ltd: Chichester, UK, 2009. [CrossRef]
62. Capasso, F.; Sirtori, C.; Cho, A.Y. Coupled quantum well semiconductors with giant electric field tunable nonlinear optical properties in the infrared. *IEEE J. Quantum Electron.* **1994**, *30*, 1313–1326. [CrossRef]
63. Lima, F.M.S.; Amato, M.A.; Nunes, O.A.C.; Fonseca, A.L.A.; Enders, B.G.; Da Silva, E.F. Unexpected transition from single to double quantum well potential induced by intense laser fields in a semiconductor quantum well. *J. Appl. Phys.* **2009**, *105*, 123111. [CrossRef]